ACSNANO

www.acsnano.org

ARTICLE

Stoichiometry-Tunable Synthesis and Magnetic Property Exploration of Two-Dimensional Chromium Selenides

Fangfang Cui, Kun He, Shengqiang Wu, Hongmei Zhang, Yue Lu, Zhenzhu Li, Jingyi Hu, Shuangyuan Pan, Lijie Zhu, Yahuan Huan, Bo Li, Xidong Duan, Qingqing Ji,* Xiaoxu Zhao,* and Yanfeng Zhang*

Cite This: https://doi.org/10.1021/acsnano.3c10609

Read Online

ACCESS | Metrics & More | Article Recommendations | Supporting Information

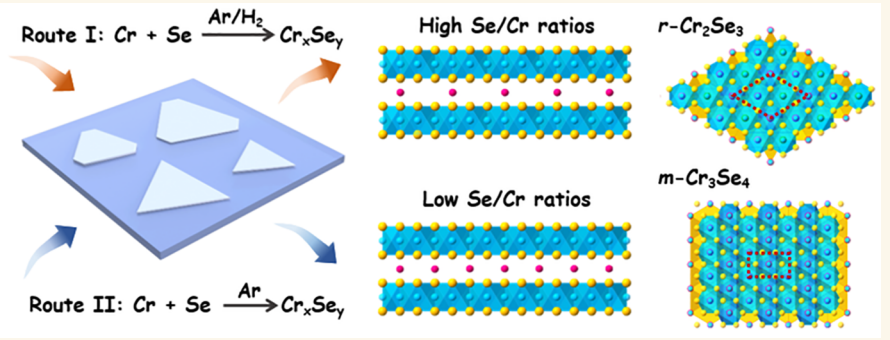

ABSTRACT: Emerging 2D chromium-based dichalcogenides (CrX_n (X = S, Se, Te; $0 < n \leq 2$)) have provoked enormous interests due to their abundant structures, intriguing electronic and magnetic properties, excellent environmental stability, and great application potentials in next generation electronics and spintronics devices. Achieving stoichiometry-controlled synthesis of 2D CrX_n is of paramount significance for such envisioned investigations. Herein, we report the stoichiometry-controlled syntheses of 2D chromium selenide (Cr_xSe_y) materials (rhombohedral Cr_2Se_3 and monoclinic Cr_3Se_4) via a Cr-self-intercalation route by designing two typical chemical vapor deposition (CVD) strategies. We have also clarified the different growth mechanisms, distinct chemical compositions, and crystal structures of the two type materials. Intriguingly, we reveal that the ultrathin Cr_2Se_3 nanosheets exhibit a metallic feature, while the Cr_3Se_4 nanosheets present a transition from *p*-type semiconductor to metal upon increasing the flake thickness. Moreover, we have also uncovered the ferromagnetic properties of 2D Cr_2Se_3 and Cr_3Se_4 below ~70 K and ~270 K, respectively. Briefly, this research should promote the stoichiometric-ratio controllable syntheses of 2D magnetic materials, and the property explorations toward next generation spintronics and magneto-optoelectronics related applications.

KEYWORDS: *chromium selenide, stoichiometry-tunable synthesis, CVD, electronic property, magnetic property*

INTRODUCTION

Since the discovery of long-range magnetic order in low-dimensional systems,[1,2] two-dimensional (2D) magnetic materials have spurred a surge of interest in the fields of fundamental physics and material sciences.[3−6] The intrinsic ferromagnetic (FM) order of 2D magnetic materials can be preserved at the unit-cell thickness, which provides an ideal platform for exploring and manipulating intriguing magnetism and other physical phenomena in the ultimate 2D limit, such as quantum anomalous Hall effect,[7−9] magneto-optic effect,[10,11] tunneling magnetoresistance,[12−14] spin−orbit torque,[15−17] skyrmion, *etc.*[18,19]

The magnetism of ultrathin 2D magnets is greatly related to the layer thickness,[2,8,20] stacking order,[21−23] *etc.* For instance,

Received: October 28, 2023
Revised: February 1, 2024
Accepted: February 7, 2024

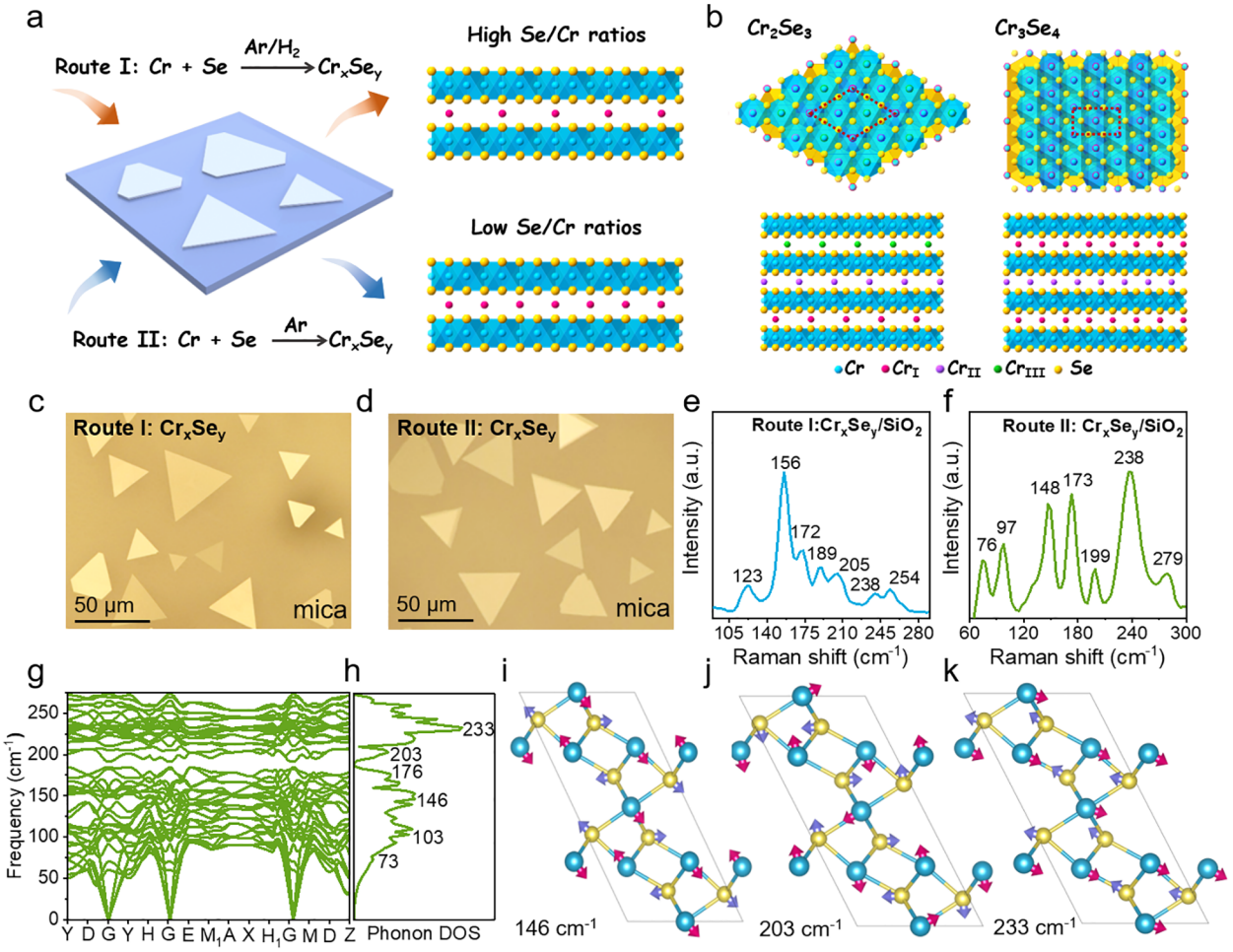

Figure 1. Synthesis and characterization of two typical Cr-intercalated Cr_xSe_y compounds via different APCVD routes (with and without H_2 promoter). (a) Schematic diagram of two typical reaction pathways, with (route-I) and without (route-II) the aid of H_2 promoter for achieving two types Cr_xSe_y nanosheets. (b) Top and side views of the atomic models for rhombohedral Cr_2Se_3 and monoclinic Cr_3Se_4. (c, d) Optical microscopy (OM) images of two types of CVD-derived Cr_xSe_y nanosheets on mica. (e, f) Disparate Raman spectra of the two types of CVD-grown 2D Cr_xSe_y nanosheets transferred on SiO_2/Si. The different Raman characteristic peaks possibly reveal their different crystal structures. (g, h) DFT-calculated phonon dispersion and corresponding density of states spectra for *m*-Cr_3Se_4. (i–k) Visualized vibrational modes peaking at 146, 203, and 233 cm^{-1} in the phonon DOS, respectively.

even/odd layer-dependent magnetic states were demonstrated in exfoliated CrI_3[2] and $CuCrSe_2$,[20] due to different interlayer magnetic coupling. Ferromagnetism and antiferromagnetism properties were uncovered in H-type and R-type stacked bilayer $CrBr_3$, respectively.[21] Moreover, external fields (*e.g.*, magnetic, electric, and electrostatic fields), strain, and heterogeneous interfaces, *etc.*[24−32] were also reported to modulate the magnetization direction, coercivity, Curie temperature (T_C), magnetic anisotropy and magnetization intensity, *etc.* Specifically, exfoliated few-layer FM semiconducting $Cr_2Ge_2Te_6$ presented bipolar gate-tuned magnetism via electrostatic gating.[28] The coercive field and Curie temperature of the exfoliated van der Waals (vdW) magnet of Fe_3GeTe_2 increased under a uniaxial tensile strain.[29] However, the above-mentioned materials systems usually suffer from unsatisfactory air stability, thickness or stacking geometry control, *etc.*, and the external field controls are rather complex.

Finding intrinsic 2D magnetic materials and developing efficient synthetic methods should be another reliable pathway. Very recently, various 2D transition metal dichalcogenides (TMDs), including VX_n,[33−36] FeX_n,[37−40] and CrX_n (X = S, Se, Te; $0 < n \leq 2$),[41−48] have been achieved to show intrinsic magnetic properties. Among these, 2D CrX_n materials have attracted special attention for their abundant structures, excellent environmental stability, high Curie temperatures, and marvelous physical properties.[9,49−54] CrX_n compounds are a kind of metal self-intercalation-induced materials, where the intercalated atoms occupied the octahedral vacancies in the vdW gaps.[42−45,48−51] The proportion of self-intercalated Cr atoms is expected to tailor the stoichiometric state and phase structure, affording diversified physical properties.

2D Cr_xSe_y compounds presented rich components ($CrSe_2$, Cr_2Se_3, Cr_3Se_4, and CrSe), high Curie temperatures, and excellent environmental stability, *etc.*,[43,48,53−56] offering great opportunities to explore the distinctive magnetic properties in the 2D limit. However, at present, only a few of them have been synthesized, such as CrSe, $CrSe_2$, and Cr_2Se_3.[43,48,53] In particular, theoretical calculations predicted that ultrathin Cr_3Se_4 with two different oxidation-states of Cr ions should possess higher Curie temperature, larger perpendicular magnetic moments, and sizable magnetocrystalline anisotropy energy than other structural analogues.[55] However, this

https://doi.org/10.1021/acsnano.3c10609
ACS Nano XXXX, XXX, XXX−XXX

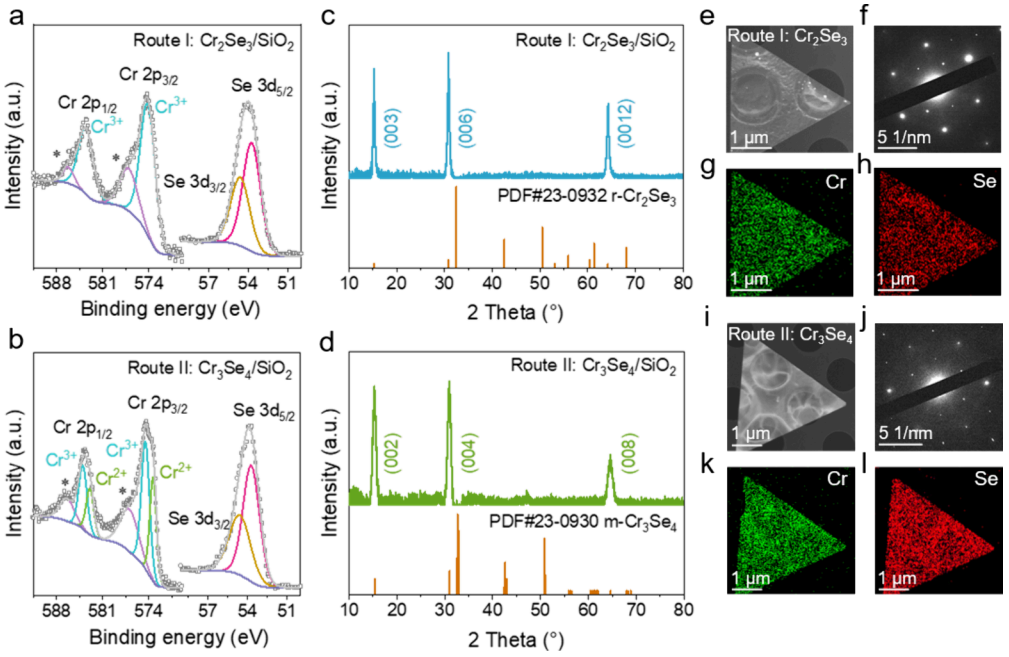

Figure 2. Element composition and structure characterizations of the two types CVD-grown Cr_xSe_y nanosheets. (a, b) XPS spectra for Cr 2p and Se 3d of (a) H_2-assisted route-I and (b) non-H_2-assisted route-II derived Cr_xSe_y nanosheets transferred on SiO_2/Si, respectively, indicating their possible compositions of Cr_2Se_3 and Cr_3Se_4. (c, d) XRD patterns of the two types nanosheets on SiO_2/Si, respectively. The orange vertical lines are the standard CIF card of the rhombohedral Cr_2Se_3 (simplified as *r*-Cr_2Se_3) and monoclinic Cr_3Se_4 (simplified as *m*-Cr_3Se_4) crystals, respectively. This analysis can be used as side evidence for addressing the different chemical compositions of Cr_2Se_3 and Cr_3Se_4. (e, i) Low-magnification TEM images of (e) route-I derived Cr_2Se_3 and (i) route-II derived Cr_3Se_4 triangular flakes. (f, j) Corresponding SAED patterns captured from route-I derived Cr_2Se_3 flake in (e) and route-II derived Cr_3Se_4 flake in (i). (g, h) EDS mapping of Cr and Se elements captured from route-I derived Cr_2Se_3 flake in (e). (k, l) EDS mapping of Cr and Se elements captured from route-II derived Cr_3Se_4 flake in (i). Homogenous chemical composition and single crystalline property can be inferred for the CVD-derived Cr_2Se_3 and Cr_3Se_4 flakes by the TEM analyses.

ultrathin 2D material has not been achieved experimentally, due to the minor chemical composition difference among the Cr_xSe_y-based materials and the failure to design delicate synthetic routes.

Herein, we report the stoichiometry-tunable synthesis of nonlayered 2D Cr_xSe_y by a facile ambient pressure chemical vapor deposition method (APCVD). Two typical reaction pathways, with and without the aid of H_2 promoter, have been designed to modulate the stoichiometric ratios of Cr and Se. Especially, the H_2 promoter is introduced to promote the cracking of Se_8 molecular rings from the evaporation of Se solid precursor, thus improving the amount and reactivity of the active Se species. The internal modulation mechanism, distinct chemical compositions, and crystal structures of the derived 2D Cr_xSe_y with different stoichiometric states will be revealed with the aid of multiscale characterization techniques. In addition, their magnetic and electrical properties will also be examined to unravel the stoichiometry-dependent ferromagnetic and electronic properties. Overall, this research is expected to propel the stoichiometry-tunable synthesis, the related physical property explorations, and the versatile applications of 2D CrX_n materials in next-generation electronic and spintronic devices.

RESULTS AND DISCUSSION

Considering the different ratios of Se in the Cr_xSe_y compounds, two typical synthetic routes were designed for tuning the precursor concentrations of the Se reactive radicals in the APCVD process. In route I, both H_2 and Ar carrier gases were introduced during the CVD synthetic process for achieving a high Se/Cr ratio. As reported previously, H_2 always functions as a cracking agent in decomposing the molecular ring of Se_8, boosting the generation of reactive Se radicals, and thus ensuring a Se-sufficient reaction environment.[57] In contrast, only Ar carrier gas was employed in route II. The schematic diagram and the experimental setup for the CVD growth of two types of Cr_xSe_y nanosheets are depicted in Figure 1a,b, and Figure S1 in the Supporting Information. Herein, chromium (Cr) and selenium (Se) powders were utilized as reactants. NaCl was introduced to lower the melting point of metal Cr reactant, facilitating its volatilization at a relatively low temperature.[41,58] The growth temperature was fixed at ~950 °C, and the growth time was ~15 min.

As shown in Figure 1c and d, triangular and hexagonal shaped Cr_xSe_y nanosheets can be successfully synthesized on mica substrates both via H_2 and non-H_2-assisted CVD routes, respectively. The corresponding optical microscopy images of Cr_xSe_y flakes transferred on SiO_2/Si templates are listed in Figure S2a,b. The domain sizes of Cr_xSe_y flakes are mainly concentrated in the range of ~20−60 μm, with the largest up to ~180 μm (Figure S2c). Besides, the thicknesses of Cr_xSe_y flakes grown in the two routes can be as thin as ~3.8 nm, as confirmed by atomic force microscopy (AFM) analysis in Figure S3.

Raman spectroscopy characterizations were first carried out to distinguish the structural information on the two types CVD-derived Cr_xSe_y nanosheets (Figure 1e,f). As for the H_2-assisted (route-I) CVD-derived Cr_xSe_y nanosheets (~20 nm thick), the characteristic Raman peaks appear at ~123, ~156, ~172, ~189, ~205, ~238, and ~254 cm^{-1} (Figure 1e),

https://doi.org/10.1021/acsnano.3c10609
ACS Nano XXXX, XXX, XXX−XXX

matching well with that of Cr_2Se_3 (~152, ~172, ~183, ~201, and ~233 cm^{-1}).[53,59] These minor deviations in peak positions should be ascribed to the thickness dependence of these Raman modes, as has been documented by previous reports.[42,50] In contrast, Raman peaks for non-H_2-assisted (route-II) CVD-derived Cr_xSe_y nanosheets (~17 nm thick) show seven primary Raman characteristic peaks at ~76, ~97, ~148, ~173, ~199, ~238, and ~279 cm^{-1} (Figure 1f), distinct from that of previously reported CrSe (~251 and ~284 cm^{-1}),[43] $CrSe_2$ (~169 and ~250 cm^{-1}),[53] and Cr_2Se_3 (~152, ~172, ~183, ~201, and ~233 cm^{-1}).[53,59] This possibly corresponds to the formation of another type Cr_xSe_y compound under the normal CVD route, namely Cr_3Se_4, as has been experimentally demonstrated in the following part of this work. Thickness-dependent Raman spectra of two types Cr_xSe_y are also displayed in Figure S4, and the different peak positions further confirm their diverse structures. Additionally, our phonon dispersion calculations (Figure 1g–k for Cr_3Se_4, and Figure S5 for Cr_2Se_3) based on density functional theory (DFT) further reveal the details of these Raman modes by visualizing the atomic displacements for relevant phonon bands (Figure 1i–k). Overall, two types Cr_xSe_y nanosheets (herein, Cr_2Se_3, Cr_3Se_4) can be achieved with the designed CVD routes with (route-I) and without (route-II) the aid of H_2 promoter.

As mentioned above, Se vapor is mainly composed of Se_8 molecules upon initial evaporation. With increasing temperature (above ~548 K), Se_8 molecules will decompose into Se_{8-x} reactive radicals, mostly into multimers, such as Se_4 or Se_2,[57] possessing relatively low concentration and chemical reactivity. Notably, the H_2 carrier gas can function as a cracking agent to decompose Se_8 molecules, producing highly reactive Se monomer radicals.[57] Thus, the concentration and reactivity of Se radicals can be increased by importing H_2 carrier, which may result in the formation of high Se/Cr ratio Cr_xSe_y compound. To exclude the metal precursor amount effect, the mass of metal Cr powder was varied obviously (from ~16 to ~24 mg), with the Se powder mass fixed (at ~300 mg). Notably, this variation of Cr mass ratio does not change the chemical composition or phase state of both CVD-derived products (Figures S6 and S7).

The impact of H_2 concentration on the growth of ultrathin Cr_xSe_y nanosheets was also systematically investigated (Figure S8). As a result, as the H_2 concentration is in the range of 0.5–2.0 sccm, both Cr_2Se_3 and Cr_3Se_4 nanosheets can be simultaneously obtained on the mica substrate, and the proportion of Cr_2Se_3 nanosheets increases as the H_2 concentration increases. Notably, only Cr_2Se_3 nanosheets can be obtained under a higher H_2 concentration (>2.0 sccm). Briefly, the H_2 promoter should be the key for mediating the stoichiometric ratios of Cr and Se in the CVD growth of Cr_xSe_y materials.

The elemental composition of two types of CVD-derived Cr_xSe_y nanosheets was then determined by X-ray photoelectron spectroscopy (XPS). The primary signals of Cr and Se can be observed from the XPS survey data and fine spectra (Figure 2a,b, and Figure S9). The peaks of Cr_2Se_3 located at ~574.4 and 583.7 eV are attributed to that of Cr $2p_{3/2}$ and Cr $2p_{1/2}$, respectively, consistent with the reported results for CVD-derived Cr_2Se_3 nanosheets.[54] While for the Cr_3Se_4 nanosheets, mixed Cr^{2+} and Cr^{3+} valence states should be observed, as predicted by previous theory calculations.[55] Herein, the observed peaks of Cr $2p_{3/2}$ (~574.5 eV) and Cr $2p_{1/2}$ (~583.9 eV) are in line with that of Cr^{3+},[54] and the peaks around ~573.4 eV (Cr $2p_{3/2}$) and ~582.9 eV (Cr $2p_{1/2}$) are assigned to be that of Cr^{2+}, since the binding energies of Cr $2p_{3/2}$ and Cr $2p_{1/2}$ were reported at ~573.6 eV and ~583.1 eV for Cr^{2+}, respectively.[60] Notably, the satellite peaks observed in the Cr(2p) XPS spectrum should arise from localized oxidation caused by residual organic compounds on the sample surface. The average valence state of Cr in Cr_3Se_4 nanosheets is ~2.5. The peaks at ~53.7 and 54.6 eV correspond to those of Se $3d_{5/2}$ and Se $3d_{3/2}$, respectively. The Cr and Se stoichiometric ratios are 1:1.52 and 1:1.33 via the H_2- and non-H_2-assisted routes, respectively, close to that of Cr_2Se_3 and Cr_3Se_4.

The structures of derived Cr_2Se_3 and Cr_3Se_4 nanosheets were further clarified by X-ray diffraction (XRD) measurements. As shown in Figure 2c and d, three dominant diffraction peaks can be observed both in Cr_2Se_3 and Cr_3Se_4 nanosheets. The first two diffraction peaks of the two types Cr_xSe_y nanosheets are located at almost identical positions, while the third diffraction peak of Cr_3Se_4 nanosheets shifts slightly to the large angle direction. Further analysis based on the standard CIF card reveals that, the diffraction peaks of the route-I derived sample located at ~15.3°, 30.9°, and 64.2° are assigned to the (003), (006), and (0012) planes of rhombohedral Cr_2Se_3 (*r*-Cr_2Se_3) (Figure 2c). The diffraction peaks of type-II samples positioned at ~15.3°, 31.0°, and 64.6°, indexed as (002), (004), and (008) planes of monoclinic Cr_3Se_4 (*m*-Cr_3Se_4) (Figure 2d). Accordingly, the Cr_xSe_y nanosheets synthesized via the designed routes, with and without the aid of H_2 promoter, are proposed to be *r*-Cr_2Se_3 and *m*-Cr_3Se_4, respectively.

Transmission electron microscopy (TEM) and energy-dispersive X-ray spectroscopy (EDS) measurements were then performed on transferred Cr_2Se_3 and Cr_3Se_4 nanosheets on Cu grids (Figure 2e,i). The EDS spectra shown in Figure S10a,b provide the atomic elemental ratios of Cr/Se for Cr_2Se_3 and Cr_3Se_4 nanosheets (*i.e.*, ~1:1.51 and 1:1.34), which is in good agreement with that of the XPS results. Uniform spatial distributions of Cr and Se elements throughout the entire flakes (Figure 2g,h and k,l) indicate the high crystalline quality of the CVD-derived Cr_2Se_3 and Cr_3Se_4 nanosheets, respectively. Besides, the selected area electron diffraction (SAED) patterns collected from Cr_2Se_3 and Cr_3Se_4 nanosheets both display a single set of spots (Figure 2f,j), highly indicative of their single-crystalline feature.

Annular dark-field scanning transmission electron microscopy (ADF-STEM) measurements were then conducted to unravel the atomic structure of the CVD-grown *m*-Cr_3Se_4 and *r*-Cr_2Se_3 nanosheets. A typical atomic-resolution ADF-STEM image of *m*-Cr_3Se_4 nanosheets along the [001] zone axis is listed in Figure 3a, where two kinds of Z contrast atoms can be unambiguously identified, with the bright atoms representing Se, and the dim atoms corresponding to Cr atoms, respectively. The corresponding simulated STEM image utilizing the *m*-Cr_3Se_4 model further verifies these experimental data (Figure 3b). The alternating bright and dim atom arrangements along the purple line in the zoom-in experimental data (Figure 3b) agree well with that of the Se–Se–Cr–Se–Se–Cr atomic array of the simulated *m*-Cr_3Se_4 model (Figure 3c). Moreover, for the *m*-Cr_3Se_4 crystal, the interlayer-intercalated Cr atoms (labeled as Cr_I and Cr_{II}, highlighted with red and purple colors, respectively) select a periodic *ab* stacking order underneath the Cr atomic sites (intralayer Cr atoms, highlighted with blue color) with a filling rate of ~50%, which results in the

https://doi.org/10.1021/acsnano.3c10609
ACS Nano XXXX, XXX, XXX–XXX

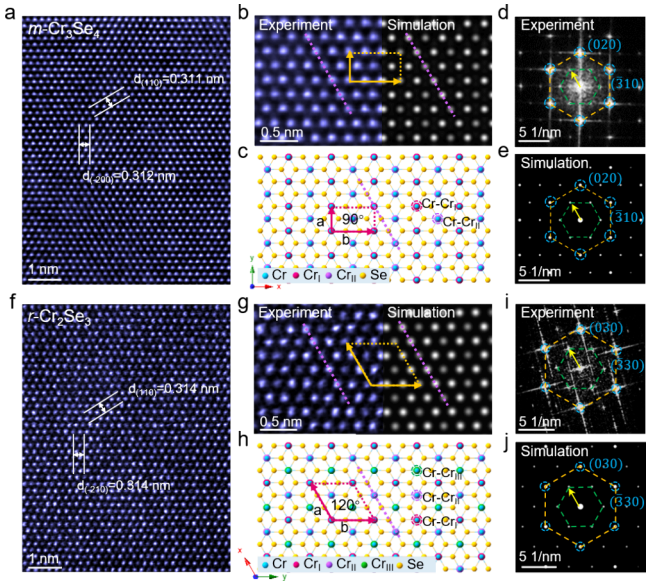

Figure 3. ADF-STEM analyses for convincing the atomic structures of m-Cr_3Se_4 and r-Cr_2Se_3 nanosheets. (a, f) Atomic-resolution ADF-STEM images of (a) m-Cr_3Se_4 and (f) r-Cr_2Se_3 nanosheets along the [001] direction. (b) Zoom-in ADF-STEM on (a), with the corresponding simulated STEM image of m-Cr_3Se_4 depicted on the right side. (g) Zoom-in ADF-STEM on (f), with the corresponding simulated STEM image of r-Cr_2Se_3 crystal displayed on the right side. (c, h) Atomic model of (c) m-Cr_3Se_4 and (h) r-Cr_2Se_3 crystals. (d) Corresponding FFT patterns of (a). (i) Corresponding FFT patterns of (f). (e, j) Simulated SAED patterns of (e) m-Cr_3Se_4 and (j) r-Cr_2Se_3 crystals along the [001] direction. The calculated lattice spacing values for Cr_3Se_4 and Cr_2Se_3 are approximately $d_{(110)}$ = 0.311 nm ($d_{(-200)}$ = 0.312 nm) and $d_{(110)}$ = 0.314 nm ($d_{(-210)}$ = 0.314 nm), respectively, consistent with the model values of $d_{(110)}$ = 0.310 nm ($d_{(-210)}$ = 0.311 nm) and $d_{(110)}$ = 0.313 nm ($d_{(-200)}$ = 0.313 nm) for Cr_3Se_4 and Cr_2Se_3, respectively.

formation of $1 \times \sqrt{3}$ $CrSe_2$ supercell, and an equivalent intensity contribution to the projected Cr atom blobs in the $CrSe_2$ framework (Figure 3c). Such ordered arrangements of the interlayer-intercalated Cr atoms can generate periodic superspots in the reciprocal space, as confirmed by both the fast Fourier transform (FFT) pattern (Figure 3d, with the superspots marked by a green hexagon), and the simulated SAED pattern (Figure 3e, ICSD 42703).[61] Further cross-section STEM images also reveal the atomic structures of m-Cr_3Se_4 nanosheets along the [130] and [110] zone axis, as illustrated in Figure S11.

Although two kinds of Z contrast atoms are visualized in the ADF-STEM image of r-Cr_2Se_3 nanosheets along the [001] zone axis (Figure 3f), the projected Cr columns of r-Cr_2Se_3 nanosheets show slightly dimmer-like contrast in contrast with that of m-Cr_3Se_4 (Figure 3a) (as indicated by the intensity line profiles (Figure S12) of purple dashed lines in Figure 3b,g), owing to the smaller amount of Cr atoms intercalated in the van der Waals gap of layered $CrSe_2$ (~33.3% occupation rate). The experimental STEM image of r-Cr_2Se_3 exhibits an identical Z contrast with that of the simulated STEM image (Figure 3g). The Se−Se−Cr−Se−Se−Cr atomic chain along the purple line in the zoom-in experimental image agrees well with that of the atomic model of r-Cr_2Se_3 crystal (Figure 3h). Besides, owing to the periodic *abc* stacking order of intercalated Cr atoms (labeled as Cr_I, Cr_{II}, and Cr_{III}, highlighted with red, purple, and green colors, respectively, Figure 3h), the FFT patterns of r-Cr_2Se_3 nanosheets show a distinct superstructure pattern of $\sqrt{3}a \times \sqrt{3}a$ (Figure 3i), which is in line with the simulated SAED result (Figure 3j, ICSD 42705).[61] The periodic arrangements of interlayer-intercalated Cr atoms are further verified according to the cross-section STEM image along the [100] and [110] zone axis (Figure S13). These analysis results further confirm the successful synthesis of r-Cr_2Se_3 and m-Cr_3Se_4 nanosheets with and without the H_2-assisted CVD processes, respectively.

2D CrX_n materials with different stoichiometric ratios may exhibit diversified physical properties. Systematically investigating the electrical and magnetic properties of nanothick Cr_2Se_3 and Cr_3Se_4 flakes is the key step. Herein, the electrical properties of 2D Cr_2Se_3 and Cr_3Se_4 nanosheets were examined by constructing back-gate field-effect transistor (FET) devices. A common linear and symmetric relationship of the output characteristic curves (drain-source current (I_{ds}) vs. drain-source voltage (V_{ds}) curves) was achieved in Cr_2Se_3- and Cr_3Se_4-based devices (Figure 4a−d, and Figures S15 and S16). This indicates that ohmic contacts are formed at the source and drain electrodes, and the electrons can well transfer between electrodes and channels.

A nontunable feature of I_{ds} under V_g (gate voltage) varying from −80 V to +80 V was obtained in various Cr_2Se_3-based devices with varied channel thicknesses (~5.0, ~5.6, ~7.3, ~7.9, ~9.6, and ~19.6 nm). This reflects the metallic property of 2D Cr_2Se_3 nanosheets (Figure 4a,b and Figures S14 and S15). This metallic feature is also convinced by scanning tunneling spectroscopy (STM) and photoelectron spectroscopy measurements of molecular beam epitaxy (MBE) grown samples, and reconfirmed by density functional theory (DFT) calculations.[62]

Intriguingly, the Cr_3Se_4-based devices manifest apparent thickness-dependent conduction behaviors, according to the output and transfer characteristic curves (Figure 4c−f and Figure S16). Specifically, the I_{ds} of ~4.4 nm and ~5.0 nm thick Cr_3Se_4-based FETs decrease with V_g varying from −80 V to +80 V (Figure 4c,e and Figure S16a,b), reflecting their *p*-type semiconducting properties. With increasing the thickness of Cr_3Se_4 flakes to ~6.1 nm and ~6.7 nm, the modulation of I_{ds} by V_g becomes weaker (Figure S16c−f). With the thickness approaching ~9.0 nm and above, a nontunable feature of I_{ds} under varying V_g is visible, revealing the metallic property of 2D Cr_3Se_4 flakes (Figure 4d,f and Figure S16g,h). The temperature-dependent resistivity of m-Cr_3Se_4 nanosheets is further examined (Figure 4h,i). Typically, for ultrathin Cr_3Se_4 nanoflakes at ~5.5 nm, the resistivity decreases as the sample temperature increases (Figure 4h), highly indicating the semiconducting feature. As for thicker Cr_3Se_4 nanoflakes (~60.0 nm), the resistivity increases as temperature increases (Figure 4i), highly indicative of its metal feature. Briefly, the CVD-derived Cr_3Se_4 nanosheets present an intriguing transition from *p*-type semiconductor to metal with increasing flake thickness (Figure 4g). This enables 2D Cr_3Se_4 nanosheets both as channel and electrode materials for manufacturing all 2D-materials-based devices. The good environmental stability of transferred Cr_2Se_3 and Cr_3Se_4 nanosheets was also characterized after being placed in air for about 3 months. As shown in Figure S17, the invariable XRD and Raman spectra highly suggest the robust stability of ultrathin Cr_2Se_3 and Cr_3Se_4 nanosheets.

The magnetic properties of various Cr_2Se_3 (in the range of ~40−47 nm thick, Figure S18a) and Cr_3Se_4 films (in the range

https://doi.org/10.1021/acsnano.3c10609
ACS Nano XXXX, XXX, XXX−XXX

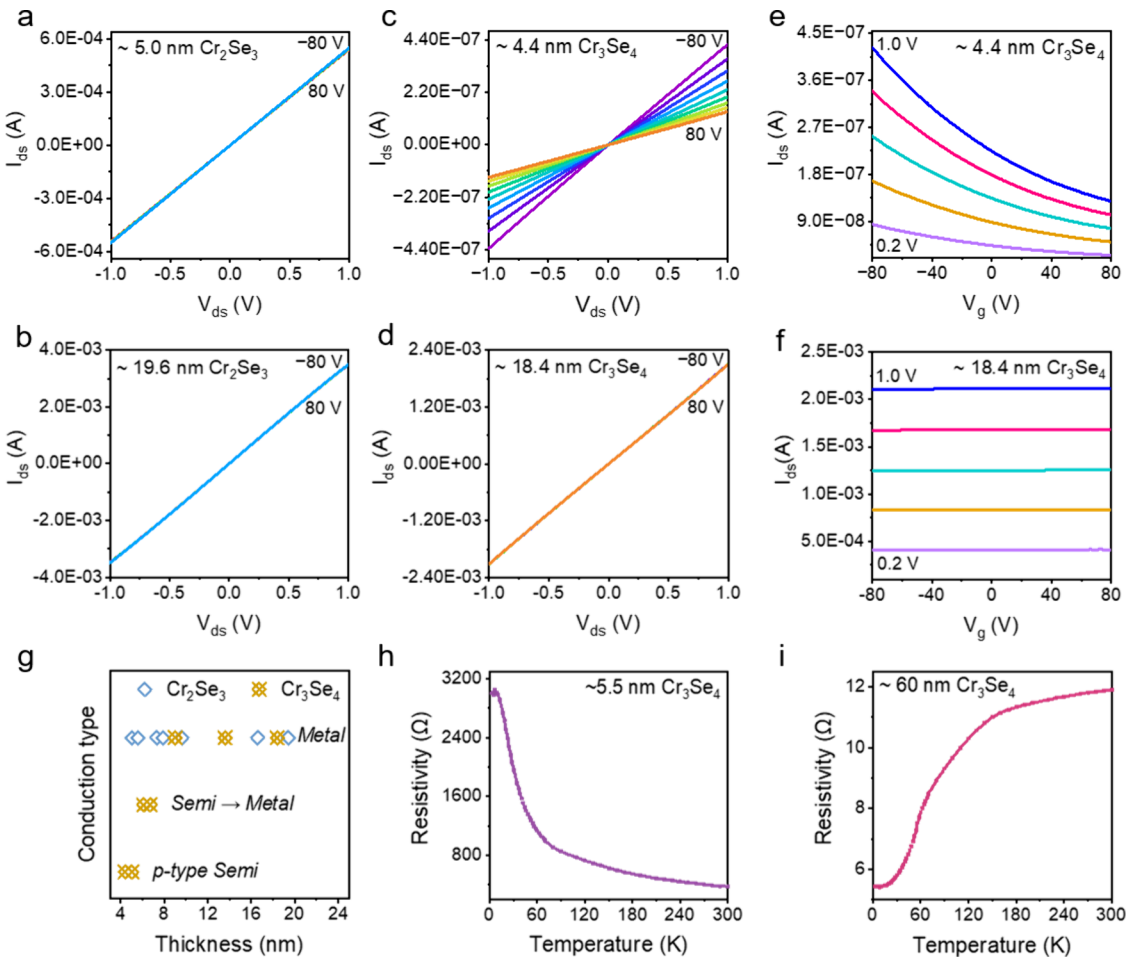

Figure 4. Electrical property characterizations of nanothick Cr_2Se_3- and Cr_3Se_4-based back-gate field-effect transistor (FET) devices. (a, b) $I_{ds}-V_{ds}$ output curves of (a) ~5.0 nm and (b) ~19.6 nm thick Cr_2Se_3-based devices. (c–f) $I_{ds}-V_{ds}$ output curves and $I_{ds}-V_g$ transfer curves of (c, e) ~4.4 nm and (d, f) ~18.4 nm thick Cr_3Se_4-based devices. (g) Summary of the conduction behaviors of Cr_2Se_3- and Cr_3Se_4-based devices with varying the thickness from ~5.0 to 19.6 nm and ~4.4 to 18.4 nm, respectively, revealing the metallic feature of Cr_2Se_3 nanosheets, and a transition of Cr_3Se_4 nanosheets from *p*-type semiconductor to metal with increasing the thickness. (i) Temperature-dependent resistivity of (h) ~5.5 nm and (i) ~60.0 nm thick Cr_3Se_4-based devices.

of ~22–35 nm thick, Figure S18b) on Al_2O_3 substrates were also explored by vibrating sample magnetometer (VSM) measurements. As shown in Figure S19, the Al_2O_3 substrate exhibits a flat VSM signal under magnetic field, reflecting the diamagnetic nature. Moreover, temperature-dependent magnetic moments measurements were also performed on Cr_2Se_3 and Cr_3Se_4 nanosheets to examine their magnetic ordering. The ZFC-FC magnetization curves of Cr_2Se_3 (Figure 5a) and Cr_3Se_4 nanosheets (Figure 5b) show obvious ferromagnetic behaviors with the T_C of ~70 K and ~270 K, respectively. Below this temperature, spontaneous magnetization exceeds the thermal fluctuation-induced net magnetic moment, and the long-range magnetic order emerges. As shown in Figure 5c,d, and Figure S20, typical magnetic hysteresis loops of Cr_2Se_3 and Cr_3Se_4 nanosheets occur below ~70 K and ~270 K, respectively. Such hysteresis reflects the spontaneous magnetization and thus the long-range ferromagnetic ordering, which is consistent with the ZFC-FC curves. Notably, the absence of sharp switching magnetization curves should be attributed to the nonuniform material thicknesses, or the introduction of surface residues during the sample preparation processes. The CVD-synthesized 2D Cr_3Se_4 (22–35 nm thick, metallic property) and Cr_2Se_3 (40–47 nm thick, metallic property) nanosheets in this work present the ferromagnetic behavior, which is consistent with that of the theoretical predictions of the ferromagnetic property in thin-layer Cr_3Se_4 and Cr_2Se_3 nanosheets.[55,56] Note that the magnetic properties of ultrathin semiconducting Cr_3Se_4 at the 2D limit (down to several nanometers or even thinner) remain unknown. And this may rely on the development of synthetic routes like the molecular beam epitaxy (MBE) route. In contrast, the bulk-state Cr_3Se_4 and Cr_2Se_3 synthesized via the chemical vapor transport method in the literature was reported to be antiferromagnets.[63,64] The difference in magnetic between bulk and ultrathin Cr_xSe_y is probably attributed to the competition between direct-exchange and superexchange/double-exchange interactions (usually favoring antiferromagnetic and ferromagnetic arrangements, respectively). In the 2D Cr_xSe_y crystals, the superexchange/double-exchange interaction should play a major role and induce the ferromagnetic arrangement. Conversely, the direct-exchange interaction should dominate in bulk Cr_xSe_y crystals due to the enhanced interlayer coupling. This results in predominant interlayer magnetic coupling behavior, and thus antiferromagnetic ordering in bulk Cr_xSe_y crystals.

https://doi.org/10.1021/acsnano.3c10609
ACS Nano XXXX, XXX, XXX–XXX

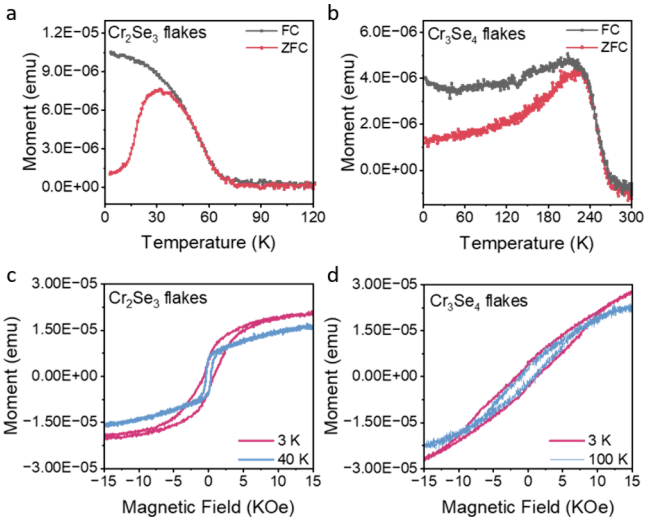

Figure 5. Magnetic property characterizations of 2D Cr_2Se_3 (in the range of ~40−47 nm thick, metallic property) and Cr_3Se_4 (in the range of ~22−35 nm thick, metallic property) nanosheets. (a, b) Temperature-dependent magnetization of Cr_2Se_3 and Cr_3Se_4 nanosheets transferred on sapphire substrates. ZFC (red) and FC (black) stand for zero-field cooling and field cooling processes, respectively. (c) Magnetization hysteresis loops of 2D Cr_2Se_3 nanosheets at temperatures of ~3 K and ~40 K, respectively. (d) Magnetization hysteresis loops of 2D Cr_3Se_4 nanosheets at temperatures of ~3 K and ~100 K, respectively. The magnetic property measurements reveal the ferromagnetism of CVD-derived Cr_2Se_3 and Cr_3Se_4, with the T_C of ~70 K and ~270 K, respectively.

The difference in T_C between Cr_2Se_3 and Cr_3Se_4 is possibly due to the different exchange interactions that drive them to produce long-range magnetic order. As predicted by previous theory calculations,[55,56] the ferromagnetic order in Cr_2Se_3 was related to the superexchange interaction occurring in the connected Cr^{3+}−X−Cr^{3+} atomic chain.[56] While for thin-layer Cr_3Se_4, in addition to the superexchange interaction between nearest-neighboring Cr atoms with the same valence (Cr^{3+}−X−Cr^{3+}), a stronger double-exchange interaction also occurs between the connected Cr^{2+} and Cr^{3+} ions according to the previous calculations.[55] The coexistence of these two type exchange interactions is hereby proposed to induce enhanced FM coupling and high T_C. Accordingly, the CVD-derived Cr_2Se_3 and Cr_3Se_4 nanosheets both present ferromagnetic properties, good air stability, and high T_C, which enable them as promising candidate materials for spintronics-related applications in next-generation integrated circuits.

CONCLUSION

In summary, we have realized the stoichiometry-tunable synthesis of 2D Cr_xSe_y materials, *i.e.*, rhombohedral Cr_2Se_3 and monoclinic Cr_3Se_4, through the design of H_2- and non-H_2-assisted CVD pathways. Intriguingly, the ultrathin Cr_2Se_3 presents a metallic feature, while Cr_3Se_4 shows a transition from *p*-type semiconductor to metal with increasing the nanosheet thickness, enabling them either as channel or electrode materials for fabricating all 2D-materials-based devices. Moreover, 2D Cr_2Se_3 and Cr_3Se_4 both exhibit intrinsic magnetism, thus providing rich material foundation for exploring spin physics in the 2D limit. Briefly, this research should propel the stoichiometry-controlled synthesis of 2D TMDs materials, and provide realistic materials to construct next-generation electronic and spintronic devices.

EXPERIMENTAL SECTION

CVD Synthesis of 2D Cr_3Se_4 and Cr_2Se_3 Nanosheets. Both types of nanosheets were synthesized in a three-zone tubular furnace equipped with a 1-in. diameter quartz tube at the atmospheric pressure CVD process. Commercial selenium powder (99.5%, Alfa), NaCl crystal, and chromium powder (99. 5%, 3AChem) were placed at the upstream, first heating zone and heating center of the tube furnace, where the temperatures were set at ~300 °C, ~880 °C, and ~950 °C, respectively. Freshly cleaved mica substrate was placed over the graphite boat. The growth in both routes was conducted at the temperature of ~950 °C for ~15 min.

Fundamental Property Characterizations. The CVD-derived samples were characterized by Optical microscope (Olympus BX51), AFM (Bruker, Dimension Icon), XPS (Kratos Analytical AXIS-Ultra with monochromatic Al Kα X-ray), Raman spectroscopy (WiTec Alpha 300R, excitation wavelength of 532 nm), XRD (D/MAX-PC 2500), TEM (JEOL JEM-2100F LaB6; acceleration voltage of 200 kV), and STEM (JEOL ARM200F, acceleration voltage, 80 kV).

Device Fabrications and Electrical Property Measurements. The CVD-derived Cr_3Se_4 and Cr_2Se_3 nanosheets were transferred onto SiO_2/Si substrates via poly(methyl methacrylate) (PMMA)-assisted transfer approach for further device fabrications. The back-gated devices were constructed through electron-beam lithography and electron-beam deposition of Ti/Au electrodes (~5/60 nm). The electrical properties were measured with a probe station (Lake Shore, Model TTP4) by using a semiconductor parameter analyzer (Keithley 4200-SCS).

Magnetic Property Measurements. The magnetic properties of transferred Cr_3Se_4 and Cr_2Se_3 nanosheets on Al_2O_3 substrates were explored by vibrating sample magnetometer (VSM) measurements. The diamagnetic signal of the Al_2O_3 substrate was eliminated.

ASSOCIATED CONTENT

Supporting Information

The Supporting Information is available free of charge at https://pubs.acs.org/doi/10.1021/acsnano.3c10609.

Additional details regarding schematic growth processes, XPS spectra, EDS spectra, Raman spectra, DFT calculations, OM images, cross-section STEM image, AFM images, electrical and magnetic measurements of Cr_2Se_3 and Cr_3Se_4 nanosheets (PDF)

AUTHOR INFORMATION

Corresponding Authors

Qingqing Ji − *School of Physical Science and Technology, ShanghaiTech University, Shanghai 201210, P. R. China;* orcid.org/0000-0001-5526-3746; Email: jiqq@shanghaitech.edu.cn

Xiaoxu Zhao − *School of Materials Science and Engineering, Peking University, Beijing 100871, P. R. China;* orcid.org/0000-0001-9746-3770; Email: xiaoxuzhao@pku.edu.cn

Yanfeng Zhang − *School of Materials Science and Engineering, Peking University, Beijing 100871, P. R. China;* orcid.org/0000-0003-1319-3270; Email: yanfengzhang@pku.edu.cn

Authors

Fangfang Cui − *School of Materials Science and Engineering, Peking University, Beijing 100871, P. R. China*

https://doi.org/10.1021/acsnano.3c10609
ACS Nano XXXX, XXX, XXX−XXX

Kun He − *College of Semiconductors (College of Integrated Circuits), School of Physics and Electronics, Hunan University, Changsha 410082, P. R. China*
Shengqiang Wu − *School of Materials Science and Engineering, Peking University, Beijing 100871, P. R. China;* orcid.org/0000-0002-3302-5445
Hongmei Zhang − *State Key Laboratory for Chemo/Biosensing and Chemometrics, College of Chemistry and Chemical Engineering, Hunan University, Changsha 410082, P. R. China*
Yue Lu − *School of Physical Science and Technology, ShanghaiTech University, Shanghai 201210, P. R. China*
Zhenzhu Li − *Department of Materials, Imperial College London, London SW7 2AZ, U.K.;* orcid.org/0000-0002-6669-563X
Jingyi Hu − *Academy for Advanced Interdisciplinary Studies and School of Materials Science and Engineering, Peking University, Beijing 100871, P. R. China*
Shuangyuan Pan − *School of Materials Science and Engineering, Peking University, Beijing 100871, P. R. China*
Lijie Zhu − *School of Materials Science and Engineering, Peking University, Beijing 100871, P. R. China*
Yahuan Huan − *School of Materials Science and Engineering, Peking University, Beijing 100871, P. R. China*
Bo Li − *College of Semiconductors (College of Integrated Circuits), School of Physics and Electronics, Hunan University, Changsha 410082, P. R. China;* orcid.org/0000-0002-5802-7519
Xidong Duan − *State Key Laboratory for Chemo/Biosensing and Chemometrics, College of Chemistry and Chemical Engineering, Hunan University, Changsha 410082, P. R. China;* orcid.org/0000-0002-4951-901X

Complete contact information is available at: https://pubs.acs.org/10.1021/acsnano.3c10609

Notes

The authors declare no competing financial interest.

ACKNOWLEDGMENTS

The work was financially supported by the National Natural Science Foundation of China (Nos. 51925201, 51991340, 51991344, 52273279, 52202157, 22205142), the National Key Research and Development Program of China (Nos. 2021YFA1202901, 2018YFA0703701), the Fundamental Research Funds for the Central Universities, and the Science and Technology Commission of Shanghai Municipality (Nos. 21ZR1442100, 21PJ1410200).

REFERENCES

(1) Gong, C.; Li, L.; Li, Z.; Ji, H.; Stern, A.; Xia, Y.; Cao, T.; Bao, W.; Wang, C.; Wang, Y.; Qiu, Z. Q.; Cava, R. J.; Louie, S. G.; Xia, J.; Zhang, X. Discovery of intrinsic ferromagnetism in two-dimensional van der Waals crystals. *Nature* **2017**, *546*, 265−269.
(2) Huang, B.; Clark, G.; Navarro-Moratalla, E.; Klein, D. R.; Cheng, R.; Seyler, K. L.; Zhong, D.; Schmidgall, E.; McGuire, M. A.; Cobden, D. H.; Yao, W.; Xiao, D.; Jarillo-Herrero, P.; Xu, X. Layer-dependent ferromagnetism in a van der Waals crystal down to the monolayer limit. *Nature* **2017**, *546*, 270−273.
(3) Fei, Z.; Huang, B.; Malinowski, P.; Wang, W.; Song, T.; Sanchez, J.; Yao, W.; Xiao, D.; Zhu, X.; May, A. F.; Wu, W.; Cobden, D. H.; Chu, J.-H.; Xu, X. Two-dimensional itinerant ferromagnetism in atomically thin Fe_3GeTe_2. *Nat. Mater.* **2018**, *17*, 778−782.
(4) Gibertini, M.; Koperski, M.; Morpurgo, A. F.; Novoselov, K. S. Magnetic 2D materials and heterostructures. *Nat.Nanotechnol.* **2019**, *14*, 408−419.
(5) Huang, B.; McGuire, M. A.; May, A. F.; Xiao, D.; Jarillo-Herrero, P.; Xu, X. Emergent phenomena and proximity effects in two-dimensional magnets and heterostructures. *Nat. Mater.* **2020**, *19*, 1276−1289.
(6) Tang, M.; Huang, J.; Qin, F.; Zhai, K.; Ideue, T.; Li, Z.; Meng, F.; Nie, A.; Wu, L.; Bi, X.; Zhang, C.; Zhou, L.; Chen, P.; Qiu, C.; Tang, P.; Zhang, H.; Wan, X.; Wang, L.; Liu, Z.; Tian, Y.; Iwasa, Y.; Yuan, H. Continuous manipulation of magnetic anisotropy in a van der Waals ferromagnet via electrical gating. *Nat. Electron.* **2022**, *6*, 28−36.
(7) Deng, Y.; Yu, Y.; Shi, M.; Guo, Z.; Xu, Z.; Wang, J.; Chen, X.; Zhang, Y. Quantum anomalous Hall effect in intrinsic magnetic topological insulator $MnBi_2Te_4$. *Science* **2020**, *367*, 895−900.
(8) Deng, Y.; Xiang, Z.; Lei, B.; Zhu, K.; Mu, H.; Zhuo, W.; Hua, X.; Wang, M.; Wang, Z.; Wang, G.; Tian, M.; Chen, X. Layer-Number-Dependent Magnetism and Anomalous Hall Effect in van der Waals Ferromagnet Fe_5GeTe_2. *Nano Lett.* **2022**, *22*, 9839−9846.
(9) Tang, B.; Wang, X.; Han, M.; Xu, X.; Zhang, Z.; Zhu, C.; Cao, X.; Yang, Y.; Fu, Q.; Yang, J.; Li, X.; Gao, W.; Zhou, J.; Lin, J.; Liu, Z. Phase engineering of Cr_5Te_8 with colossal anomalous Hall effect. *Nat. Electron.* **2022**, *5*, 224−232.
(10) Sun, Z.; Yi, Y.; Song, T.; Clark, G.; Huang, B.; Shan, Y.; Wu, S.; Huang, D.; Gao, C.; Chen, Z.; McGuire, M.; Cao, T.; Xiao, D.; Liu, W.-T.; Yao, W.; Xu, X.; Wu, S. Giant nonreciprocal second-harmonic generation from antiferromagnetic bilayer CrI_3. *Nature* **2019**, *572*, 497−501.
(11) Liu, Z.; Guo, K.; Hu, G.; Shi, Z.; Li, Y.; Zhang, L.; Chen, H.; Zhang, L.; Zhou, P.; Lu, H.; Lin, M.; Liu, S.; Cheng, Y.; Liu, X. L.; Xie, J.; Bi, L.; Tan, P.; Deng, L.; Qiu, C.; Peng, B. Observation of nonreciprocal magnetophonon effect in nonencapsulated few-layered CrI_3. *Sci. Adv.* **2020**, *6*, eabc7628.
(12) Song, T.; Cai, X.; Tu, M. W-Y; Zhang, X.; Huang, B.; Wilson, N. P.; Seyler, K. L.; Zhu, L.; Taniguchi, T.; Watanabe, K.; McGuire, M. A.; Cobden, D. H.; Di, X.; Yao, W.; Xu, X. Giant tunneling magnetoresistance in spin-filter van der Waals heterostructures. *Science* **2018**, *360*, 1214−1218.
(13) Wang, Z.; Gutiérrez-Lezama, I.; Ubrig, N.; Kroner, M.; Gibertini, M.; Taniguchi, T.; Watanabe, K.; Imamoğlu, A.; Giannini, E.; Morpurgo, A. F. Very large tunneling magnetoresistance in layered magnetic semiconductor CrI_3. *Nat. Commun.* **2018**, *9*, 2516.
(14) Zhu, W.; Lin, H.; Yan, F.; Hu, C.; Wang, Z.; Zhao, L.; Deng, Y.; Kudrynskyi, Z. R.; Zhou, T.; Kovalyuk, Z. D.; Zheng, Y.; Patanè, A.; Žutić, I.; Li, S.; Zheng, H.; Wang, K. Large Tunneling Magnetoresistance in van der Waals Ferromagnet/Semiconductor Heterojunctions. *Adv. Mater.* **2021**, *33*, 2104658.
(15) Alghamdi, M.; Lohmann, M.; Li, J.; Jothi, P. R.; Shao, Q.; Aldosary, M.; Su, T.; Fokwa, B. P. T.; Shi, J. Highly Efficient Spin−Orbit Torque and Switching of Layered Ferromagnet Fe_3GeTe_2. *Nano Lett.* **2019**, *19*, 4400−4405.
(16) Ostwal, V.; Shen, T.; Appenzeller, J. Efficient Spin-Orbit Torque Switching of the Semiconducting Van Der Waals Ferromagnet $Cr_2Ge_2Te_6$. *Adv. Mater.* **2020**, *32*, 1906021.
(17) Wang, Q.; Zeng, Y.; Yuan, K.; Zeng, Q.; Gu, P.; Xu, X.; Wang, H.; Han, Z.; Nomura, K.; Wang, W.; Liu, E.; Hou, Y.; Ye, Y. Magnetism modulation in $Co_3Sn_2S_2$ by current-assisted domain wall motion. *Nat. Electron.* **2023**, *6*, 119−125.
(18) Li, B.; Deng, X.; Shu, W.; Cheng, X.; Qian, Q.; Wan, Z.; Zhao, B.; Shen, X.; Wu, R.; Shi, S.; Zhang, H.; Zhang, Z.; Yang, X.; Zhang, J.; Zhong, M.; Xia, Q.; Li, J.; Liu, Y.; Liao, L.; Ye, Y.; Dai, L.; Peng, Y.; Li, B.; Duan, X. Air-stable ultrathin Cr_3Te_4 nanosheets with thickness-dependent magnetic biskyrmions. *Mater. Today* **2022**, *57*, 66−74.
(19) Zhang, C.; Liu, C.; Zhang, S.; Zhou, B.; Guan, C.; Ma, Y.; Algaidi, H.; Zheng, D.; Li, Y.; He, X.; Zhang, J.; Li, P.; Hou, Z.; Yin, G.; Liu, K.; Peng, Y.; Zhang, X. X. Magnetic Skyrmions with Unconventional Helicity Polarization in a Van Der Waals Ferromagnet. *Adv. Mater.* **2022**, *34*, 2204163.

(20) Peng, J.; Su, Y.; Lv, H.; Wu, J.; Liu, Y.; Wang, M.; Zhao, J.; Guo, Y.; Wu, X.; Wu, C.; Xie, Y. Even-odd-layer-dependent Ferromagnetism in Two-dimensional Non-van der Waals $CrCuSe_2$. *Adv. Mater.* **2023**, *35*, 2209365.
(21) Chen, W.; Sun, Z.; Wang, Z.; Gu, L.; Xu, X.; Wu, S.; Gao, C. Direct observation of van der Waals stacking−dependent interlayer magnetism. *Science* **2019**, *366*, 983−987.
(22) Jiang, P.; Wang, C.; Chen, D.; Zhong, Z.; Yuan, Z.; Lu, Z.-Y.; Ji, W. Stacking tunable interlayer magnetism in bilayer CrI_3. *Phys. Rev. B* **2019**, *99*, 144401.
(23) Song, T.; Fei, Z.; Yankowitz, M.; Lin, Z.; Jiang, Q.; Hwangbo, K.; Zhang, Q.; Sun, B.; Taniguchi, T.; Watanabe, K.; McGuire, M. A.; Graf, D.; Cao, T.; Chu, J.-H.; Cobden, D. H.; Dean, C. R.; Xiao, D.; Xu, X. Switching 2D magnetic states via pressure tuning of layer stacking. *Nat. Mater.* **2019**, *18*, 1298−1302.
(24) Deng, Y.; Yu, Y.; Song, Y.; Zhang, J.; Wang, N. Z.; Sun, Z.; Yi, Y.; Wu, Y. Z.; Wu, S.; Zhu, J.; Wang, J.; Chen, X. H.; Zhang, Y. Gate-tunable room-temperature ferromagnetism in two-dimensional Fe_3GeTe_2. *Nature* **2018**, *563*, 94−99.
(25) Huang, B.; Clark, G.; Klein, D. R.; MacNeill, D.; Navarro-Moratalla, E.; Seyler, K. L.; Wilson, N.; McGuire, M. A.; Cobden, D. H.; Xiao, D.; Yao, W.; Jarillo-Herrero, P.; Xu, X. Electrical control of 2D magnetism in bilayer CrI_3. *Nat. Nanotechnol.* **2018**, *13*, 544−548.
(26) Jiang, S.; Shan, J.; Mak, K. F. Electric-field switching of two-dimensional van der Waals magnets. *Nat. Mater.* **2018**, *17*, 406−410.
(27) Jiang, S.; Li, L.; Wang, Z.; Mak, K. F.; Shan, J. Controlling magnetism in 2D CrI_3 by electrostatic doping. *Nat. Nanotechnol.* **2018**, *13*, 549−553.
(28) Wang, Z.; Zhang, T.; Ding, M.; Dong, B.; Li, Y.; Chen, M.; Li, X.; Huang, J.; Wang, H.; Zhao, X.; Li, Y.; Li, D.; Jia, C.; Sun, L.; Guo, H.; Ye, Y.; Sun, D.; Chen, Y.; Yang, T.; Zhang, J.; Ono, S.; Han, Z.; Zhang, Z. Electric-field control of magnetism in a few-layered van der Waals ferromagnetic semiconductor. *Nat. Nanotechnol.* **2018**, *13*, 554−559.
(29) Wang, Y.; Wang, C.; Liang, S. J.; Ma, Z.; Xu, K.; Liu, X.; Zhang, L.; Admasu, A. S.; Cheong, S. W.; Wang, L.; Chen, M.; Liu, Z.; Cheng, B.; Ji, W.; Miao, F. Strain-Sensitive Magnetization Reversal of a van der Waals Magnet. *Adv. Mater.* **2020**, *32*, 2004533.
(30) Zhong, J.; Wang, M.; Liu, T.; Zhao, Y.; Xu, X.; Zhou, S.; Han, J.; Gan, L.; Zhai, T. Strain-sensitive ferromagnetic two-dimensional Cr_2Te_3. *Nano Res.* **2022**, *15*, 1254−1259.
(31) Cenker, J.; Sivakumar, S.; Xie, K.; Miller, A.; Thijssen, P.; Liu, Z.; Dismukes, A.; Fonseca, J.; Anderson, E.; Zhu, X.; Roy, X.; Xiao, D.; Chu, J.-H.; Cao, T.; Xu, X. Reversible strain-induced magnetic phase transition in a van der Waals magnet. *Nat. Nanotechnol.* **2022**, *17*, 256−261.
(32) Gong, C.; Zhang, X. Two-dimensional magnetic crystals and emergent heterostructure devices. *Science* **2019**, *363*, 706.
(33) Bonilla, M.; Kolekar, S.; Ma, Y.; Diaz, H. C.; Kalappattil, V.; Das, R.; Eggers, T.; Gutierrez, H. R.; Phan, M.-H.; Batzill, M. Strong room-temperature ferromagnetism in VSe_2 monolayers on van der Waals substrates. *Nat. Nanotechnol.* **2018**, *13*, 289−293.
(34) Wong, P. K. J.; Zhang, W.; Bussolotti, F.; Yin, X.; Herng, T. S.; Zhang, L.; Huang, Y. L.; Vinai, G.; Krishnamurthi, S.; Bukhvalov, D. W.; Zheng, Y. J.; Chua, R.; N'Diaye, A. T.; Morton, S. A.; Yang, C. Y.; Ou Yang, K. H.; Torelli, P.; Chen, W.; Goh, K. E. J.; Ding, J.; Lin, M. T.; Brocks, G.; de Jong, M. P.; Castro Neto, A. H.; Wee, A. T. S. Evidence of Spin Frustration in a Vanadium Diselenide Monolayer Magnet. *Adv. Mater.* **2019**, *31*, 1901185.
(35) (35.) Yu, W.; Li, J.; Herng, T. S.; Wang, Z.; Zhao, X.; Chi, X.; Fu, W.; Abdelwahab, I.; Zhou, J.; Dan, J.; Chen, Z.; Chen, Z.; Li, Z.; Lu, J.; Pennycook, S. J.; Feng, Y. P.; Ding, J.; Loh, K. P. Chemically Exfoliated VSe_2 Monolayers with Room-Temperature Ferromagnetism. *Adv. Mater.* **2019**, *31*, 1903779.
(36) Liu, H.; Xue, Y.; Shi, J.-A.; Guzman, R. A.; Zhang, P.; Zhou, Z.; He, Y.; Bian, C.; Wu, L.; Ma, R.; Chen, J.; Yan, J.; Yang, H.; Shen, C.-M.; Zhou, W.; Bao, L.; Gao, H.-J. Observation of the Kondo Effect in Multilayer Single-Crystalline VTe_2 Nanoplates. *Nano Lett.* **2019**, *19*, 8572−8580.
(37) Kang, L.; Ye, C.; Zhao, X.; Zhou, X.; Hu, J.; Li, Q.; Liu, D.; Das, C. M.; Yang, J.; Hu, D.; Chen, J.; Cao, X.; Zhang, Y.; Xu, M.; Di, J.; Tian, D.; Song, P.; Kutty, G.; Zeng, Q.; Fu, Q.; Deng, Y.; Zhou, J.; Ariando, A.; Miao, F.; Hong, G.; Huang, Y.; Pennycook, S. J.; Yong, K.-T.; Ji, W.; Renshaw Wang, X.; Liu, Z. Phase-controllable growth of ultrathin 2D magnetic FeTe crystals. *Nat. Commun.* **2020**, *11*, 3729.
(38) Zhao, Z.; Zhou, J.; Liu, L.; Liu, N.; Huang, J.; Zhang, B.; Li, W.; Zeng, Y.; Zhang, T.; Ji, W.; Yang, T.; Zhang, Z.; Li, S.; Hou, Y. Two-Dimensional Room-Temperature Magnetic Nonstoichiometric Fe_7Se_8 Nanocrystals: Controllable Synthesis and Magnetic Behavior. *Nano Lett.* **2022**, *22*, 1242−1250.
(39) Wang, P.; Wen, Y.; Zhao, X.; Zhai, B.; Du, R.; Cheng, M.; Liu, Z.; He, J.; Shi, J. Controllable Synthesis Quadratic-Dependent Unsaturated Magnetoresistance of Two-Dimensional Nonlayered Fe_7S_8 with Robust Environmental Stability. *ACS Nano* **2022**, *16*, 8301−8308.
(40) Huan, Y.; Luo, T.; Han, X.; Ge, J.; Cui, F.; Zhu, L.; Hu, J.; Zheng, F.; Zhao, X.; Wang, L.; Wang, J.; Zhang, Y. Composition-Controllable Syntheses and Property Modulations from 2D Ferromagnetic Fe_5Se_8 to Metallic Fe_3Se_4 Nanosheets. *Adv. Mater.* **2023**, *35*, 2207276.
(41) Cui, F.; Zhao, X.; Xu, J.; Tang, B.; Shang, Q.; Shi, J.; Huan, Y.; Liao, J.; Chen, Q.; Hou, Y.; Zhang, Q.; Pennycook, S. J.; Zhang, Y. Controlled Growth and Thickness-Dependent Conduction-Type Transition of 2D Ferrimagnetic Cr_2S_3 Semiconductors. *Adv. Mater.* **2020**, *32*, 1905896.
(42) Zhou, S.; Wang, R.; Han, J.; Wang, D.; Li, H.; Gan, L.; Zhai, T. Ultrathin Non-van der Waals Magnetic Rhombohedral Cr_2S_3: Space-Confined Chemical Vapor Deposition Synthesis and Raman Scattering Investigation. *Adv. Funct. Mater.* **2019**, *29*, 1805880.
(43) Zhang, Y.; Chu, J.; Yin, L.; Shifa, T. A.; Cheng, Z.; Cheng, R.; Wang, F.; Wen, Y.; Zhan, X.; Wang, Z.; He, J. Ultrathin Magnetic 2D Single-Crystal CrSe. *Adv. Mater.* **2019**, *31*, 1900056.
(44) Wen, Y.; Liu, Z.; Zhang, Y.; Xia, C.; Zhai, B.; Zhang, X.; Zhai, G.; Shen, C.; He, P.; Cheng, R.; Yin, L.; Yao, Y.; Getaye Sendeku, M.; Wang, Z.; Ye, X.; Liu, C.; Jiang, C.; Shan, C.; Long, Y.; He, J. Tunable Room-Temperature Ferromagnetism in Two-Dimensional Cr_2Te_3. *Nano Lett.* **2020**, *20*, 3130−3139.
(45) Chua, R.; Zhou, J.; Yu, X.; Yu, W.; Gou, J.; Zhu, R.; Zhang, L.; Liu, M.; Breese, M. B. H.; Chen, W.; Loh, K. P.; Feng, Y. P.; Yang, M.; Huang, Y. L.; Wee, A. T. S. Room Temperature Ferromagnetism of Monolayer Chromium Telluride with Perpendicular Magnetic Anisotropy. *Adv. Mater.* **2021**, *33*, 2103360.
(46) Meng, L.; Zhou, Z.; Xu, M.; Yang, S.; Si, K.; Liu, L.; Wang, X.; Jiang, H.; Li, B.; Qin, P.; Zhang, P.; Wang, J.; Liu, Z.; Tang, P.; Ye, Y.; Zhou, W.; Bao, L.; Gao, H.-J.; Gong, Y. Anomalous thickness dependence of Curie temperature in air-stable two-dimensional ferromagnetic 1T-$CrTe_2$ grown by chemical vapor deposition. *Nat. Commun.* **2021**, *12*, 809.
(47) Xian, J.-J.; Wang, C.; Nie, J.-H.; Li, R.; Han, M.; Lin, J.; Zhang, W.-H.; Liu, Z.-Y.; Zhang, Z.-M.; Miao, M.-P.; Yi, Y.; Wu, S.; Chen, X.; Han, J.; Xia, Z.; Ji, W.; Fu, Y.-S. Spin mapping of intralayer antiferromagnetism and field-induced spin reorientation in monolayer $CrTe_2$. *Nat. Commun.* **2022**, *13*, 257.
(48) Luo, S.; Zhu, X.; Liu, H.; Song, S.; Chen, Y.; Liu, C.; Zhou, W.; Tang, C.; Shao, G.; Jin, Y.; Guan, J.; Tung, V. C.; Li, H.; Chen, X.; Ouyang, F.; Liu, S. Direct Growth of Magnetic Non-van der Waals Cr_2X_3(X = S, Se, and Te) on SiO_2/Si Substrates through the Promotion of KOH. *Chem. Mater.* **2022**, *34*, 2342−2351.
(49) Chen, C.; Chen, X.; Wu, C.; Wang, X.; Ping, Y.; Wei, X.; Zhou, X.; Lu, J.; Zhu, L.; Zhou, J.; Zhai, T.; Han, J.; Xu, H. Air-Stable 2D Cr_5Te_8 Nanosheets with Thickness-Tunable Ferromagnetism. *Adv. Mater.* **2022**, *34*, 2107512.
(50) Chu, J.; Zhang, Y.; Wen, Y.; Qiao, R.; Wu, C.; He, P.; Yin, L.; Cheng, R.; Wang, F.; Wang, Z.; Xiong, J.; Li, Y.; He, J. Sub-millimeter-Scale Growth of One-Unit-Cell-Thick Ferrimagnetic Cr_2S_3 Nanosheets. *Nano Lett.* **2019**, *19*, 2154−2161.
(51) Wu, H.; Zhang, W.; Yang, L.; Wang, J.; Li, J.; Li, L.; Gao, Y.; Zhang, L.; Du, J.; Shu, H.; Chang, H. Strong intrinsic room-

https://doi.org/10.1021/acsnano.3c10609
ACS Nano XXXX, XXX, XXX−XXX

temperature ferromagnetism in freestanding non-van der Waals ultrathin 2D crystals. *Nat. Commun.* **2021**, *12*, 5688.
(52) Zhang, X.; Lu, Q.; Liu, W.; Niu, W.; Sun, J.; Cook, J.; Vaninger, M.; Miceli, P. F.; Singh, D. J.; Lian, S.-W.; Chang, T.-R.; He, X.; Du, J.; He, L.; Zhang, R.; Bian, G.; Xu, Y. Room-temperature intrinsic ferromagnetism in epitaxial $CrTe_2$ ultrathin films. *Nat. Commun.* **2021**, *12*, 2492.
(53) Li, B.; Wan, Z.; Wang, C.; Chen, P.; Huang, B.; Cheng, X.; Qian, Q.; Li, J.; Zhang, Z.; Sun, G.; Zhao, B.; Ma, H.; Wu, R.; Wei, Z.; Liu, Y.; Liao, L.; Ye, Y.; Huang, Y.; Xu, X.; Duan, X.; Ji, W.; Duan, X. Van der Waals epitaxial growth of air-stable $CrSe_2$ nanosheets with thickness-tunable magnetic order. *Nat. Mater.* **2021**, *20*, 818−825.
(54) Zhu, X.; Liu, H.; Liu, L.; Ren, L.; Li, W.; Fang, L.; Chen, X.; Xie, L.; Jing, Y.; Chen, J.; Liu, S.; Ouyang, F.; Zhou, Y.; Xiong, X. Spin Glass State in Chemical Vapor-Deposited Crystalline Cr_2Se_3 Nanosheets. *Chem. Mater.* **2021**, *33*, 3851−3858.
(55) Zhang, X.; Wang, B.; Guo, Y.; Zhang, Y.; Chen, Y.; Wang, J. High Curie temperature and intrinsic ferromagnetic half-metallicity in two-dimensional Cr_3X_4 (X = S, Se, Te) nanosheets. *Nanoscale Horiz* **2019**, *4*, 859−866.
(56) He, Z.; Peng, R.; Feng, X.; Xu, X.; Dai, Y.; Huang, B.; Ma, Y. Two-dimensional valleytronic semiconductor with spontaneous spin and valley polarization in single-layer Cr_2Se_3. *Phys. Rev. B* **2021**, *104*, No. 075105.
(57) Cheng, Q.; Pang, J.; Sun, D.; Wang, J.; Zhang, S.; Liu, F.; Chen, Y.; Yang, R.; Liang, N.; Lu, X.; Ji, Y.; Wang, J.; Zhang, C.; Sang, Y.; Liu, H.; Zhou, W. WSe_2 2D p-type semiconductor-based electronic devices for information technology: Design, preparation, and applications. *InfoMat* **2020**, *2*, 656−697.
(58) Cui, F.; Zhao, X.; Tang, B.; Zhu, L.; Huan, Y.; Chen, Q.; Liu, Z.; Zhang, Y. Epitaxial Growth of Step-Like Cr_2S_3 Lateral Homojunctions Towards Versatile Conduction Polarities and Enhanced Transistor Performances. *Small* **2022**, *18*, 2105744.
(59) Hu, X.; Jin, Z.; Zhong, Y.; Dai, J.; Tao, X.; Zhang, X.; Han, J.; Jiang, S.; Zhou, L. Epitaxial Growth of Two-Dimensional Magnetic Lateral and Vertical Heterostructures. *Chem. Mater.* **2023**, *35*, 4220.
(60) Shenasa, M.; Sainkar, S.; Lichtman, D. XPS study of some selected selenium compounds. *J. Electron Spectrosc. Relat. Phemon.* **1986**, *40*, 329−337.
(61) Wehmeier, F. H.; Keve, E. T.; Abrahams, S. C. Preparation, structure, and properties of some chromium selenides. Crystal growth with selenium vapor as a novel transport agent. *Inorg. Chem.* **1970**, *9*, 2125−2131.
(62) Liu, M.; Huang, Y. L.; Gou, J.; Liang, Q.; Chua, R.; Arramel; Duan, S.; Zhang, L.; Cai, L.; Yu, X.; Zhong, D.; Zhang, W.; Wee, A. T. S. Diverse Structures and Magnetic Properties in Nonlayered Monolayer Chromium Selenide. *J. Phys. Chem. C* **2021**, *12*, 7752−7760.
(63) Ohta, S.; Adachi, Y. Covalency effects of Te substitution on the antiferromagnetic stability of $Cr_3Se_{4-y}Te_y$. *J. Magn. Magn. Mater.* **1996**, *164*, 225−232.
(64) Wu, J.; Zhang, C.-L. Z.; Yan, J.-M.; Chen, L.; Guo, L.; Chen, T.-W.; Gao, Gu-Y.; Fei, L. F.; Zhao, W. Y.; Chai, Y.; Zheng, R.-K. Magnetotransport and magnetic properties of the layered noncollinear antiferromagnetic Cr_2Se_3 single crystals. *J. Phys.: Condens. Matter* **2020**, *32*, 475801.

https://doi.org/10.1021/acsnano.3c10609
ACS Nano XXXX, XXX, XXX−XXX